ACS APPLIED NANO MATERIALS

www.acsanm.org Article

Laser-Induced Graphene Strain Sensor for Conformable Lip-Reading Recognition and Human−Machine Interaction

Lin Cheng,[‖] Guoqing Fang,[‖] Lei Wei, Weizhan Gao, Xueer Wang, Zihan Lv, Wenjie Xu, Chen Ding, Huaping Wu,* Wenan Zhang,* and Aiping Liu*

Cite This: *ACS Appl. Nano Mater.* 2023, 6, 7290−7298 Read Online

ACCESS | Metrics & More | Article Recommendations | Supporting Information

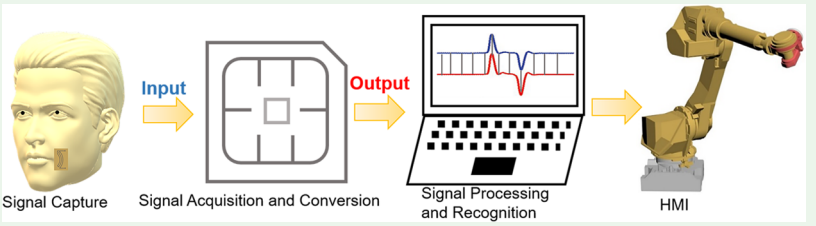

ABSTRACT: Lip-reading recognition (LRR) has gained significant attention due to its potential applications in various scenarios, such as communication for the speech-impaired, conversations in noisy or dark environments, and human−machine interactions. However, existing LRR technologies based on computer vision suffer from drawbacks such as the high cost of electronic camera equipment and the negative impact of ambient lighting on recognition accuracy. Herein, a graphene-based flexible strain sensor is developed through a facile, high-efficiency, and low-cost laser-induced carbonization technique, which involves the ablation of polyimide (PI) films using ultraviolet lasers. The sensor's patterned stripes and porous structure endow it with sensitivity to deformations caused by bending and pressing. The well-designed flexible strain sensor can tightly attach on facial skin and record high-quality strain signals of various lip muscle movements. When compared to a preconstructed lip-reading database using a fixed algorithm, the collected lip-reading signals exhibit a recognition rate exceeding 90%, enabling seamless human−machine interaction and precise control over manipulators. Consequently, the LRR approach based on the flexible strain sensor demonstrates immense potential as a promising platform for speech-impaired communication and human−machine interactions in variable environments.

KEYWORDS: *laser-induced graphene, lip-reading recognition, human−machine interaction, flexible strain sensor, lip muscle movement*

1. INTRODUCTION

Speech recognition technology has become prevalent in applications such as voice communication software, voice-controlled cars, and voice-based authentication systems. However, it is unsuitable for the speech-impaired and is susceptible to environmental noise interference. In contrast, lip-reading recognition (LRR) technology, which enables silent speech recognition,[1] has gained significant research interest in various fields, including speech-impaired communication and human−machine interaction (HMI).[2,3]

Unlike traditional speech recognition methods that rely on computer vision or millimeter-wave radar technology,[4,5] LRR is less affected by environmental noise but faces challenges in large-scale production due to complex, costly instrumentation systems, and intricate processing procedures. Additionally, computer vision-based LRR is easily influenced by ambient light, resulting in reduced recognition rates under insufficient lighting conditions. Radar-based LRR is prone to ambient electromagnetic interference, leading to ineffective recognition and feedback in communication radio wave environments.[6] Fortunately, emerging flexible strain sensors, such as electronic skins and electronic tattoos, offer promising solutions to these issues.[7−12]

These sensors can monitor various physiological strain signals,[13] including pulse, respiratory rate, and heartbeat, and can be integrated with hands, feet, and other human organs to capture electrophysiological information for HMI.[14−17] Flexible sensors attached to the face can realize effective sensing of facial expressions or lip-reading information.[18−20] However, the movement of human facial muscles are complex, for example, masseter and temporal muscles control occlusion, smile muscles control expression, and so on.[21] Hence, it is crucial to design a lip-reading strain sensor that primarily senses the lip area while remaining unaffected by the deformation of other facial muscles.

Received: January 27, 2023
Revised: April 13, 2023
Accepted: April 14, 2023
Published: May 1, 2023

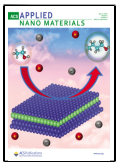

https://doi.org/10.1021/acsanm.3c00410
ACS Appl. Nano Mater. 2023, 6, 7290−7298

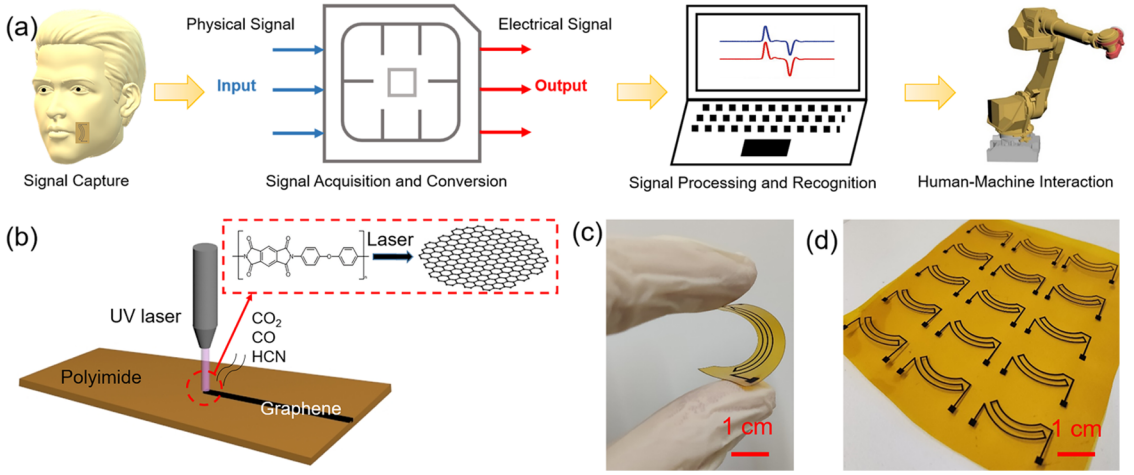

Figure 1. LIG strain sensor for LRR and HMI. (a) Schematic diagram of the signal recording system for LRR and HMI. (b) Fabrication principle of LIG. (c) LIG sensor with perfect flexibility. (d) Batch production of LIG sensors.

Graphene has recently emerged as a promising sensing material owing to its excellent mechanical and electrical properties.[22,23] To commercialize graphene, various synthesis protocols have been developed, including mechanical exfoliation, chemical vapor deposition, and chemical reduction of graphene oxide.[24−26] These methods have the advantage in manufacturing graphene of different grades, and they also present challenges, such as nonscalable production, high energy consumption, and massive waste generation.[27] Laser-induced technology has been recognized as a powerful approach for high-throughput, precisely programmable, and mask-free fabrication of various electronics, such as wearable strain sensors, heterostructure transistors, and flexible electrochemical sensors.[2,28−33] Laser-induced graphene (LIG) on polyimide (PI) substrates has also been explored for patterned strain sensors, achieving controllable physical and electrical properties and tailorable sensitivities[34,35] by precisely controlling laser power, speed, and atmosphere.[36,37] Herein, we propose a flexible lip-reading strain sensor based on the LIG. To capture the motion information of lip muscles and convert it into electrical signals that can be processed by a computer (Figure 1a), we investigate the performance of the strain sensor under different bending and pressing conditions and examine the effects of different laser parameters on its sensing capabilities. Moreover, flexible strain sensors detect signals from lip muscle movements. The LRR technology allows the device to understand and recognize language via the sensor affixed around the lips, match the electrical signal with the lip-reading database stored in the device using specific algorithms, and subsequently determine the lip-reading content. The LRR results can be displayed in a written form or interpreted by technical equipment as commands to perform specific tasks through HMI equipment in diverse environments, such as obscured, dynamic, quiet, dark, and noisy settings.[4]

2. EXPERIMENTAL SECTION

2.1. Preparation of LIG. A 50 μm thick PI film (Shenzhen Golden Green Leaf Electronic Material Co., Ltd., China, CX-PI12-250) was used as the substrate material. A laser device (model CY-ZW3W) with an ultraviolet (UV) source (laser power 3 W, laser wavelength 355 nm) was provided by Shenzhen Chaoyue Laser Intelligent Equipment Co., Ltd., China. First, the PI film was stuck on the silica gel pad without wrinkles and cleaned with ethanol. The laser parameters were set, including a focus of 4 mm above the PI film, pulse width of 1 μm, pulse frequency range from 120 to 180 kHz, scanning speed from 20 to 80 mm/s, and a scanning spacing from 0.001 to 0.02 mm. When the laser was applied to the surface of the PI film, the PI molecule's original structure was destroyed at high temperatures. Some oxygen and nitrogen atoms were released as gases, and the remaining carbon atoms formed graphene structures, as illustrated in Figure 1b. The LIG strain sensor on the plastic PI film had good flexibility (Figure 1c) and was easy to design different shapes and patterns according to complex needs (Figure 1d). Additionally, a laser device with a CO_2 laser source (Harbin Jintai Laser Technology Co., Ltd., China, JTTS-ER, laser power 20 W, laser wavelength 10.6 μm) was also used to prepare LIG as the control.

2.2. Characterization. The microstructure of the LIG sensor was analyzed by a scanning electron microscope (SEM, CARL ZEISS SMT PTE Ltd.) at an extra high voltage of 3 kV. The component and structure properties of graphene were analyzed by a Raman spectrometer (LabRAM HR Evolution, HORIBA France SAS), an X-ray photoelectron spectrometer (XPS, Kα, Thermo Fisher Scientific), and an X-ray diffractometer (XRD, D8 DISCOVER, BRUKER) using Cu Kα radiation (λ = 0.15,418 nm) with a 2θ scan from 10 to 60° at a step of 0.2°. The real-time tests of the electromechanical properties of the sensors were carried out via a two-point-probe method by using a Keithley 2400 SourceMeter.

2.3. Algorithm. The MATLAB language was used to construct similarity and recognition rate algorithms. The precollected lip-reading data was used to build a MATLAB database, and the real-time collected signal was compared with the database. Here, the Euclidean distance measurement method and Dynamic Time Warping algorithm were used for time normalization. A manipulator was controlled by the recognition results to complete specific actions.

3. RESULTS AND DISCUSSION

3.1. Effect of Laser Parameters on the Microstructure and Sensitivity of LIG Carbonized by Using UV Lasers. The most common method for producing LIG is by using CO_2 laser; nevertheless, UV lasers are better absorbed by PI films and are relatively safer as a cold light source compared to CO_2 laser. The photon energy of UV lasers matches the atomic bond energy, enabling it to directly break the chemical bonds of PI atoms, limiting significant changes in the volume during the decomposition process.[37] This allows the UV laser to create a finer sensor structure on the PI surface. As shown in Figure S1, CO_2 laser-induced graphene has a fine pore structure with a friable lamellar structure on the surface layer due to the high thermal energy of the CO_2 laser. In contrast, UV-laser-induced graphene exhibits two structural features: a

https://doi.org/10.1021/acsanm.3c00410
ACS Appl. Nano Mater. 2023, 6, 7290−7298

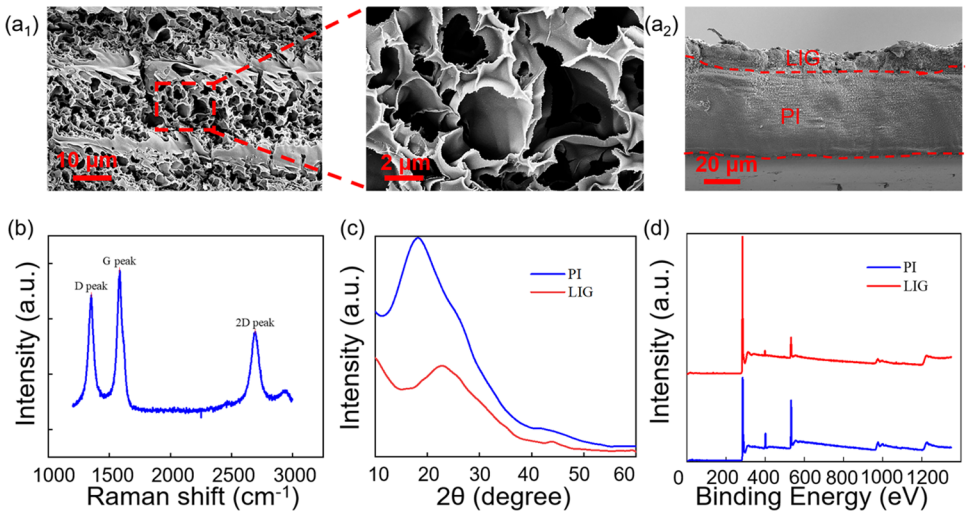

Figure 2. Morphology and microstructure of LIG. SEM images of (a_1) LIG surface and (a_2) cross section. (b) Raman spectrum of LIG. (c) XRD spectra of PI and LIG. (d) XPS spectra of PI and LIG.

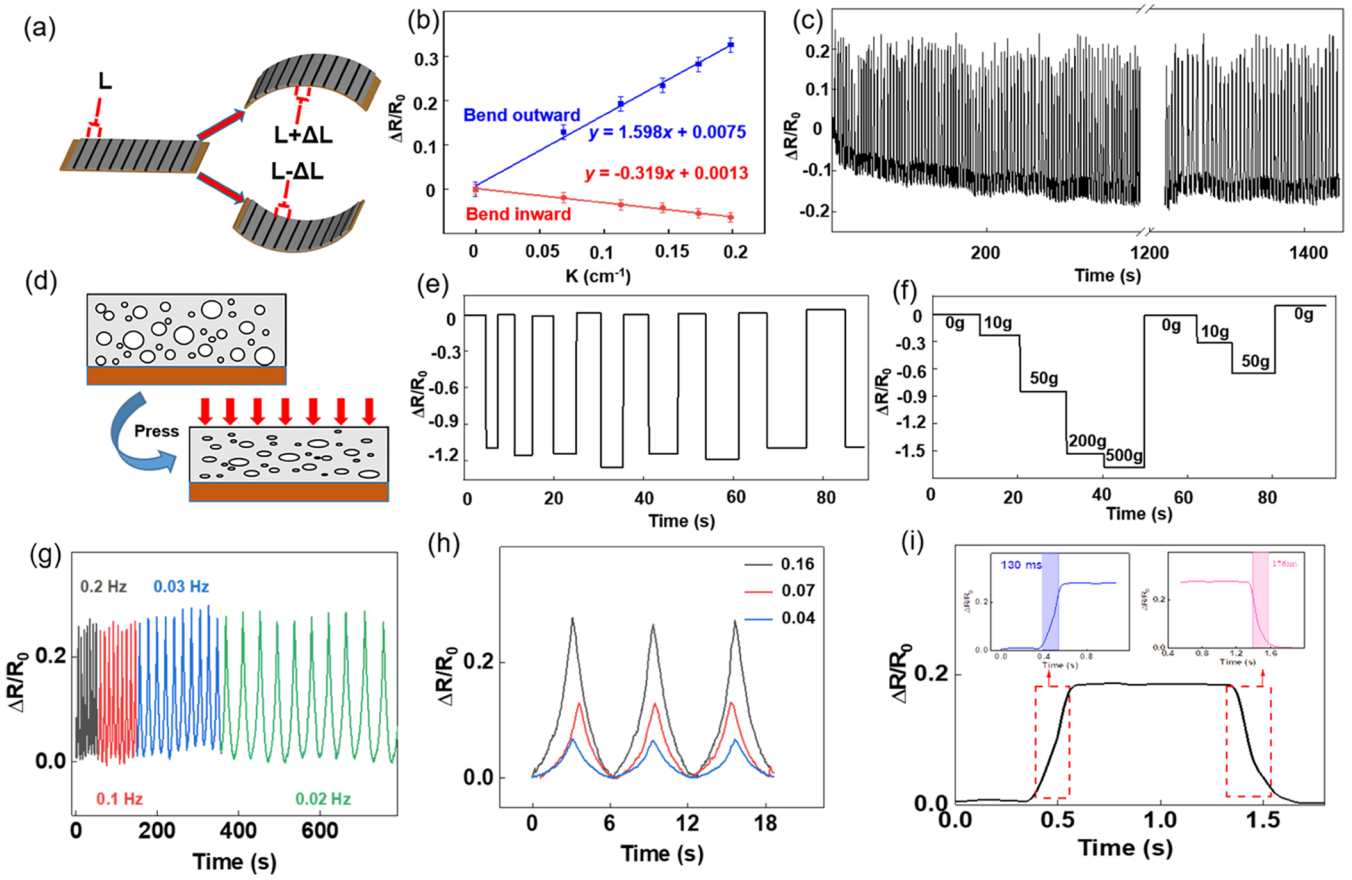

Figure 3. Sensing performances of LIG strain sensors. (a) Schematic diagram of the deformation of LIG strain sensors at bending outward and bending inward states. (b) Relative resistance changes of LIG strain sensors under different bending states. (c) Repeatability test of the sensor over 500 bending cycles. (d) Schematic diagram of deformation of LIG sensors under pressure. (e) Repeatability test of the sensor for pressure-sensitive characteristics. (f) Relative resistance changes of LIG strain sensors under different pressures. Cycle tests under (g) different bending frequencies and (h) different states. (i) Response time and recovery time.

banded structure due to laser scanning and a hierarchical porous structure (Figures 2a and S1b). The magnified SEM image of the LIG film displays that the porous size ranges from 0.5 to 4 μm (Figure 2a_1), and the thickness of the carbonized layer is about 15 μm (Figure 2a_2). Changing laser parameters can further adjust the hierarchical structure of LIG. For example, the average laser power is in direct proportion to the peak power, pulse width, and pulse frequency of the laser. When retaining the peak power and pulse width unchanged, the average laser power will increase with increasing pulse frequency. As shown in Figure S2a, as the pulse frequency increases from 130 to 170 kHz, the banded structure gradually

https://doi.org/10.1021/acsanm.3c00410
ACS Appl. Nano Mater. 2023, 6, 7290−7298

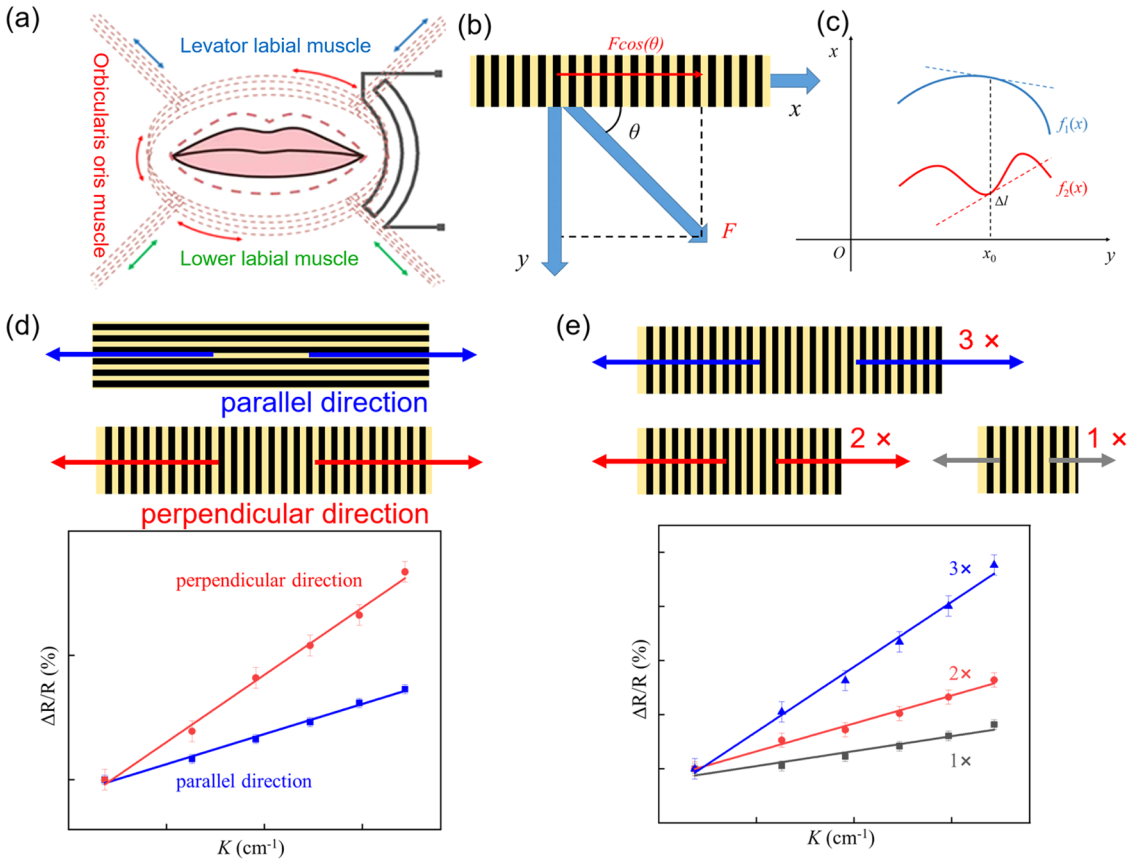

Figure 4. (a) Muscles around the lip and the design of sensors. (b) Effective force direction of the LIG strain sensor. (c) Effective length that Δl of the sensor curve f_2 maps to the muscle fiber curve f_1. (d) Sensitivity of LIG sensors to deformation along different directions. (e) Effect of stripe numbers to sensitivity of LIG sensors.

disappears, and porous structures become dominant (Figure S2a1−a3). Meanwhile, increasing the scanning speed and scanning spacing of the laser spot reduces the laser energy received by a specific point on the PI surface, resulting in a more complete and finer stripe structure (Figure S2b1−b3, c1−c3). When the scanning spacing of the laser increases to 0.02 mm, the villiform structure joined between the stripes becomes more obvious (Figure S2c3), forming another conductive path perpendicular to the LIG stripe structure. When the scanning spacing of the laser further increases to 0.03 mm, the adjacent graphene bands do not lap together, leading to a significant decrease in the conductivity in the direction perpendicular to the stripe structure of LIG. Therefore, laser parameters affect the conductivity (1.5×10^2 to 3.0×10^5 Ω·cm) and sensing performance of the LIG sensor. An excessively low laser energy results in insufficient PI ablation, sacrificing the conductivity of the LIG sensor, while an excessively high laser energy destroys the graphene structure and can even cause delamination and shedding of LIG from the PI surface. Consequently, optimizing UV laser parameters is essential for enhancing the sensing responses of the LIG sensor (Figure S3). The optimal parameters (including a pulse frequency of 150 kHz, scanning speed of 50 mm/s, scanning distance of 0.02 mm) are set for the preparation of the LIG strain sensor (Figure S2c3) in subsequent research.

Figure 2b shows the Raman spectrum of LIG obtained at optimal parameters. There are three distinct characteristic peaks of D, G, and 2D after PI laser ablation. The D peak at 1350 cm^{-1} is related to the defect or edge of LIG. The G peak at 1580 cm^{-1} and the 2D peak at 2700 cm^{-1} indicate the number of graphene layers. The intensity ratio of D peak to G peak reflects the disorder degree, crystallinity, and defects of graphene.[22,37−41] As the height of the G peak is significantly higher than that of the 2D peak, it means a multilayer structure of LIG. Figure 2c shows the XRD patterns before and after PI laser ablation. The obvious graphitization diffraction peak that appeared at around $2\theta = 24°$ is attributed to the diffraction peak of the (002) crystal plane of graphite, whose position is affected by the incomplete removal of functional groups in LIG.[42,43] In addition, the diffraction peak is wide and the intensity is weak due to the increase of disorder of LIG. The XPS spectra of PI and LIG in Figure 2d also confirm that the peak intensity of carbon increases and those of nitrogen and oxygen decrease after PI graphitization, which is in accordance with the characteristics of reduced oxygen graphene.[44,45]

3.2. Strain-Sensing Characteristics and Sensing Mechanism of the LIG Sensor. We probe into the strain-sensing characteristics of flexible LIG sensors by the bending test. The stripe-structure surface of the LIG sensor is toward the outside with the chord length of the LIG sample being controlled by a clamp with the lateral slip function (Figure S4). As the two ends of the fixture move closer, the LIG sensor exhibited either an outward bending state or an inward bending state, with adjacent bands separating or converging, as shown in Figure 3a. This results in a reduced contact area between adjacent LIG strips, increased contact resistance, and positive correlation property between the resistance change

https://doi.org/10.1021/acsanm.3c00410
ACS Appl. Nano Mater. 2023, 6, 7290−7298

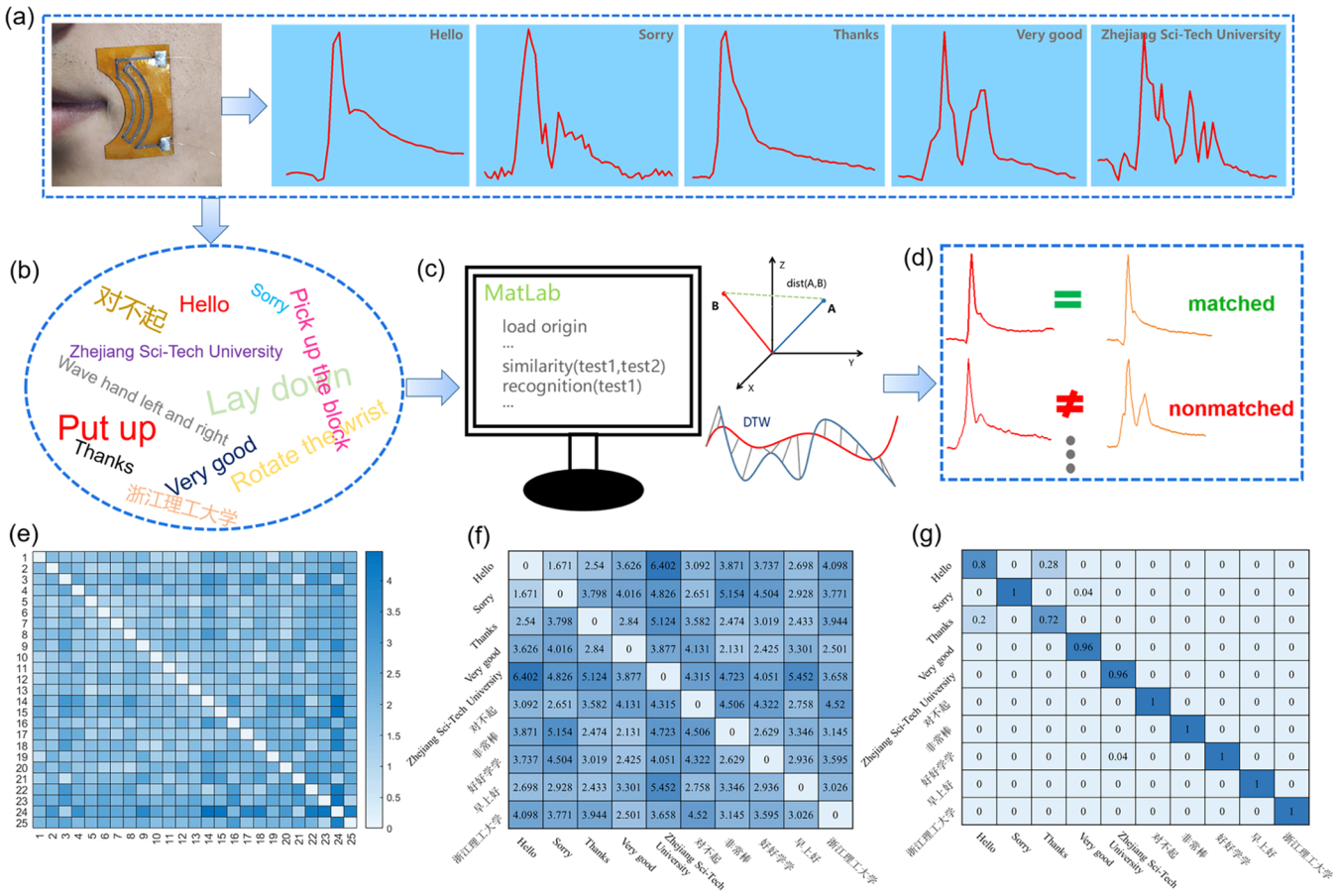

Figure 5. Implementation process of LRR. (a) Lip-reading sensor is applied to the lip to obtain signals of common English phrases. (b) Form a lip-reading database. (c) Algorithmic processing. (d) Matching recognition. (e) Horizontal comparison matrix taking "Hello" as an example. (f) Vertical comparison matrix of 10 Chinese and English phrases. (g) Recognition rate matrix of 10 phrases.

rate ($\Delta R/R_0$) and the curvature (K) of LIG strips under the outward bending state (Figure 3b), and vice versa. The strain sensor showed satisfactory repeatability, with performance remaining constant after more than 500 bending tests (Figure 3c) and a response time of 130 ms (Figure 3i). In addition, the sensor exhibited excellent cyclic stability under different bending frequencies (Figure 3g) and stable, identical signals under cyclic bending/release tests (Figure 3h). We also investigated the performance of the LIG sensor under pressure, as shown in Figure 3f. The resistance change progressively increases with increasing pressure, due to the fact that when pressure is applied, the LIG becomes denser and the contact area between adjacent graphene sheet layers in the three-dimensional (3D) porous structure increases, similar to a compressed sponge, which enhances conductivity (Figure 3d). Its stability and repeatability were verified by repeated load–unload cycle tests (Figure 3e,3f). The LIG flexible strain sensor exhibits the abovementioned superior linearity, sensitivity, and repeatability during bending and pressing. Therefore, the sensor can effectively capture and provide feedback on signals of body movements, including large movements such as arm flexion (Figure S5a), lateral wrist flexion (Figure S5b), and finger flexion (Figure S5c), as well as small movements like pulse beat (Figure S5d), breathing (Figure S6a), swallowing (Figure S6b), and vocal cord vibration (Figure S5c,d), which validates the sensor's exceptional adaptability and stability for in situ physiological signal detection.

3.3. Lip-Reading Recognition and Human-Computer Interaction via the LIG Strain Sensor. In order to realize LRR with high efficiency and high accuracy, understanding lip muscle movement during speech is crucial. As shown in Figure 4a, the orbicularis oris muscle, levator labial muscle, and lower labial muscle are distributed around the lip. The levator labial muscle and lower labial muscle control lip opening and closing, while the orbicularis oris muscle determines the lip shape. These muscles collectively influence mouth shape changes during speech, with the orbicularis oris muscle playing a dominant role. To minimize interference from facial expressions or mastication in LRR, the contraction of the orbicularis oris muscle should be a key deformation factor considered in designing LRR sensors. The shape and placement of sensors in conformity with lip muscles are particularly important for accurately measuring lip muscle movement. Our further results suggest that the deformation along the direction of LIG stripes exhibits higher sensitivity (Figure 4), and the sensitivity increases with the number of stripes (Figure 4e). Therefore, the sensor is designed to be long enough along the direction of LIG stripes (Figure 4a, perpendicular direction) but narrow enough to effectively avoid the multidirectional deformation interference of other facial muscle groups. Comprehensive consideration, the sensor should be designed as a structure parallel to the direction of the orbicularis oris muscle fiber and with repeated lines to increase the sensing length. Additionally, the direction of the repeated corners should resemble those of the levator labii and

https://doi.org/10.1021/acsanm.3c00410
ACS Appl. Nano Mater. 2023, 6, 7290−7298

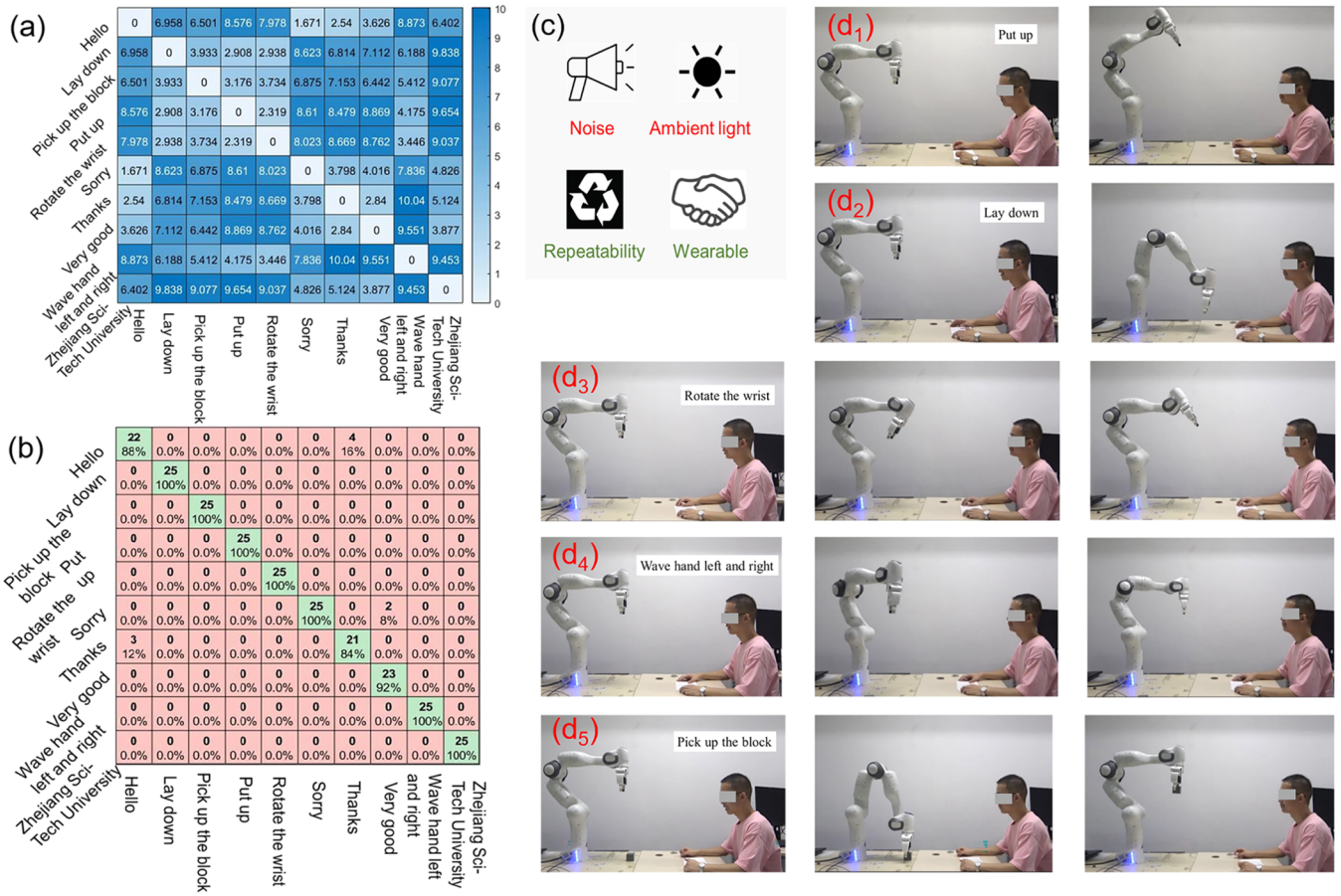

Figure 6. Implementation method of HMI. (a) Similarity matrix of manipulator control instructions. (b) Recognition rate matrix of manipulator control instructions. (c) Advantages of HMI technology based on LRR. (d) Manipulator control based on LRR.

depressor labii muscles to optimally trace lip muscle movement patterns. Herein, we designed five sensors with different shapes, affixed them to the same position of the lip, and detected the resistance change signal of lip-reading 26 English letters to evaluate the sensing performances of the five sensors (Figure S7). Notably, sensor A distinguishes more English letters and detects subtler signal changes related to lip muscle movement (Figure S7a), confirming its higher sensitivity and superior recognition capability. In addition, sensor A was subjected to cyclic bendability tests by placing it in a natural environment for 1, 7, and 21 days, and its relative resistance remained essentially unchanged, verifying its environmental adaptability and stability (Figure S8).

Consider the multistripe distribution of the LIG strain sensor, when LIG is bent or stretched under an external force F at θ angle to the x-axis, the component in the x-axis is F·cos θ (Figure 4b). According to the above discussion, the sensor sensitivity in the y-axis direction is less than that in the x-axis direction under the condition of equal length, and the sensor has a long sensing path along the x-axis direction. In addition, the small width of the sensor makes the deformation along the y-axis difficult, so only the deformation in the x-axis direction should be mainly discussed. The effective component of F is maximal only when $\theta = 0$. For an arbitrary movement curve of the muscle fiber $f_1(x)$, the sensor shape curve $f_2(x)$ can be divided into n Δl elements (Figure 4c), and the effective length of the Δl element at x_0 mapped to $f_1(x)$ can be expressed as

$$\Delta l \cos(\arctan(f_2'(x_0)) - \arctan(f_1'(x_0))) \quad (1)$$

The total effective length L can be expressed as

$$L = \Delta l \sum_{0}^{n} \cos(\theta_1 - \theta_2) \quad (2)$$

It can be seen that the more the points where $(\theta_1 - \theta_2) = 0$ among n sampling points, the greater the L value will be, that is to say, the tangent slope of the sensor electrode curve and muscle fiber curve is the same at any point x_0. In other words, when the two curves are parallel, the effective length of a sensor electrode will reach the maximum and the sensor effect will be optimal. This is consistent with our experimental results.

In order to realize LRR, the lip-reading signals related to five common English phrases ("Hello", "Sorry", "Thanks", "Very good", and "Zhejiang Sci-Tech University") and five common Chinese phrases (Figure S9) were collected by using the LIG sensor with an optimized structure (Figure S7a) when the sensor was attached to the mouth corner (Figure 5a). 25 test signals were taken from each phrase to form a database of common lip-reading phrases (Figure 5b). It can be found that different lip-reading phrases will have different waveform signals (Figure 5a). According to the MATLAB programming algorithm, the similarity and recognition rates of each lip-reading signal are tested (Figure 5c,d). In the process of data analysis, we need to know the size of individual differences and then evaluate the individual similarity. To compare the differences between X and Y individuals, we mainly use the distance measurement. The Euclidean distance is the most

https://doi.org/10.1021/acsanm.3c00410
ACS Appl. Nano Mater. 2023, 6, 7290−7298

common distance measurement, which measures the absolute distance between two points in multidimensional space.[46,47] The Euclidean distance between two n-dimensional vectors $\vec{a}(x_{11}, x_{12}, \cdots, x_{1n})$ and $\vec{b}(x_{21}, x_{22}, \cdots, x_{2n})$ is

$$d = \sqrt{\sum_{k=1}^{n} (x_{1k} - x_{2k})^2} \tag{3}$$

The dynamic time warping (DTW) algorithm uses a time warping function satisfying certain conditions to describe the time correspondence between the test template and the reference template and solves the warping function corresponding to the minimum cumulative distance when the two templates match. When the dimension or the number of sequences is different and cannot correspond to each other one by one, we need to use the DTW algorithm to expand or reduce to the same number of sequences, and then calculate the distance, as shown in Figure S10.[48−50] By limiting the boundary conditions, continuity, and monotonicity, the path with the least cost of regularization can be obtained

$$\mathrm{DTW}(Q, C) = \min\left(\sqrt{\sum_{k=1}^{K} w_k}\right)/K \tag{4}$$

Here, Q and C represent the time series of lengths n and m, respectively. The time warping path W consists of K elements. w_k represents the k-th element of the time warping path, that is the Euclidean distance between the i-th element in sequence Q and the j-th element in sequence C, $w_k = d(Q_i, C_j)$. Finally, we can use the minimum cumulative distances to represent the best path by using the algorithm

$$\gamma(i, j) = d(Q_i, C_j) + \min\{\gamma(i-1, j-1), \gamma(i-1, j), \gamma(i, j-1)\} \tag{5}$$

Here, $\gamma(i, j)$ represents cumulative distances.

Figure 5e presents a horizontal similarity matrix using "Hello" as an exemplar, while Figure 5f displays a vertical contrast matrix of 10 prevalent phrases. The color intensity indicates the waveform distance. Lighter colors can be observed in the comparison of more similar phrases. Furthermore, the recognition rate matrix of the 10 phrases can be obtained using a recognition algorithm, as shown in Figure 5g. A darker color indicates a higher recognition rate. The average recognition rate for phrases exceeds 90%, with most being fully recognized. However, there are still some phrases that can be misconstrued, such as "Hello" and "Thanks". In summary, by constructing a comprehensive lip-reading database, lip-reading recognition (LRR) technology can serve as an effective supplement to visual terminal interfaces, enabling daily communication for the deaf and mute, even in situations requiring silence or where voices are inaudible.

The LRR technology is further employed in HMI processes. Common manipulator control commands, such as "Put up," "Lay down," "Rotate the wrist," "Wave hand left and right," and "Pick up the block," are integrated with commonly used English phrases and then can be correctly identified (Figure 6a,6b). When connected to the manipulator, lip-reading commands can control the manipulator's actions (Figure 6d and Movie S1). This LRR-based HMI demonstrates durability, repeatability, and a significant reduction in environmental interference (Figure 6c). Additionally, it can be applied to surdomute communication (Movie S2) and dialogs in dark or noisy environments, offering promising prospects for complex control in variable situations.

4. CONCLUSIONS

In summary, we employed UV laser to ablate PI films to obtain the finely designed strain sensor of graphene, which presented bending and pressing sensing characteristics. The LIG sensor was used to successfully explore human limb movements and physiological signals by changing the contact areas of the stripe structure and porous structure of graphene under variable bending and compression deformation. Furthermore, by optimizing the sensor structure, the LIG strain sensor was employed to detect lip muscle movements and collect lip-reading signals, achieving a high recognition rate (up to 90%) for a lip-reading database comprising common English and Chinese phrases via the Dynamic Time Warping algorithm. LRR technology enabled HMI by controlling the manipulator's actions based on lip-reading commands, even in noisy environments, silent or surdomute communication, and dialogs in dark environments, showcasing its potential as an alternative to traditional speech and visual recognition methods.

■ ASSOCIATED CONTENT

Supporting Information

The Supporting Information is available free of charge at https://pubs.acs.org/doi/10.1021/acsanm.3c00410.

Lip-reading commands to control the movements of the manipulator (Movie S1) (MP4)

Lip-reading commands to control the movements of the manipulator in silent communication (Movie S2) (MP4)

SEM images of LIG by using CO_2 and UV lasers (Figure S1); SEM images of LIG prepared under various laser parameters (Figure S2); performance of LIG strain sensors obtained at different laser parameters (Figure S3); optical diagram of LIG strain sensors during the bending test (Figure S4); detection of various body movements by using LIG strain sensors (Figure S5); breathing, swallowing, and vocal cord vibration signals by using the LIG strain sensor (Figure S6); lip-reading sensing of 26 English letters by using five sensors with different designs (Figure S7); cyclic bendability test of sensor A in a natural environment (Figure S8); lip-reading signals of five common Chinese phrases (Figure S9); and original lip-reading and DTW time series of "hello" and "sorry" (Figure S10) (PDF)

■ AUTHOR INFORMATION

Corresponding Authors

Huaping Wu − *College of Mechanical Engineering, Zhejiang University of Technology, Hangzhou 310023, P. R. China;* orcid.org/0000-0003-4505-7062; Email: wuhuaping@gmail.com

Wenan Zhang − *College of Information Engineering, Zhejiang University of Technology, Hangzhou 310023, P. R. China;* Email: wazhang@zjut.edu.cn

Aiping Liu − *Key Laboratory of Optical Field Manipulation of Zhejiang Province, Zhejiang Sci-Tech University, Hangzhou 310018, P. R. China;* orcid.org/0000-0002-2338-062X; Email: liuaiping1979@gmail.com

https://doi.org/10.1021/acsanm.3c00410
ACS Appl. Nano Mater. 2023, 6, 7290−7298

Authors

Lin Cheng − *Key Laboratory of Optical Field Manipulation of Zhejiang Province, Zhejiang Sci-Tech University, Hangzhou 310018, P. R. China;* orcid.org/0000-0001-8680-1383

Guoqing Fang − *Key Laboratory of Optical Field Manipulation of Zhejiang Province, Zhejiang Sci-Tech University, Hangzhou 310018, P. R. China*

Lei Wei − *Key Laboratory of Optical Field Manipulation of Zhejiang Province, Zhejiang Sci-Tech University, Hangzhou 310018, P. R. China*

Weizhan Gao − *College of Information Engineering, Zhejiang University of Technology, Hangzhou 310023, P. R. China*

Xueer Wang − *College of Information Engineering, Zhejiang University of Technology, Hangzhou 310023, P. R. China*

Zihan Lv − *Key Laboratory of Optical Field Manipulation of Zhejiang Province, Zhejiang Sci-Tech University, Hangzhou 310018, P. R. China*

Wenjie Xu − *Key Laboratory of Optical Field Manipulation of Zhejiang Province, Zhejiang Sci-Tech University, Hangzhou 310018, P. R. China*

Chen Ding − *Key Laboratory of Optical Field Manipulation of Zhejiang Province, Zhejiang Sci-Tech University, Hangzhou 310018, P. R. China*

Complete contact information is available at: https://pubs.acs.org/10.1021/acsanm.3c00410

Author Contributions

‖L.C. and G.F. contributed equally to this work. The manuscript was written through contributions of all authors. All authors have given approval to the final version of the manuscript.

Notes

The authors declare no competing financial interest.

■ ACKNOWLEDGMENTS

This work was supported by the Zhejiang Outstanding Youth Fund of China (No. LR19E020004), the Youth Top-notch Talent Project of Zhejiang Ten Thousand Plan of China (No. ZJWR0308010), the National Natural Science Foundation of China (No. 12272351 and 11972323), the Zhejiang Provincial Natural Science Foundation of China (No. LR20A020002), and the Fundamental Research Funds for the Provincial Universities of Zhejiang (No. RF-B2019004).

■ REFERENCES

(1) Zhu, M.; Zhang, H.; Wang, X.; Wang, X.; Yang, Z.; Wang, C.; Samuel, O. W.; Chen, S.; Li, G. Towards optimizing electrode configurations for silent speech recognition based on high-density surface electromyography. *J. Neural Eng.* **2021**, *18*, No. 016005.

(2) Yan, Z.; Wang, L.; Xia, Y.; Qiu, R.; Liu, W.; Wu, M.; Zhu, Y.; Zhu, S.; Jia, C.; Zhu, M.; Cao, R.; Li, Z.; Wang, X. Flexible High-Resolution Triboelectric Sensor Array Based on Patterned Laser-Induced Graphene for Self-Powered Real-Time Tactile Sensing. *Adv. Funct. Mater.* **2021**, *31*, No. 2100709.

(3) Vadillo, J.; Santana, R. On the human evaluation of universal audio adversarial perturbations. *Comput. Secur* **2022**, *112*, No. 102495.

(4) Wang, Y.; Tang, T.; Xu, Y.; Bai, Y.; Yin, L.; Li, G.; Zhang, H.; Liu, H.; Huang, Y. All-weather, natural silent speech recognition via machine-learning-assisted tattoo-like electronics. *npj Flexible Electron* **2021**, *5*, No. 20.

(5) Lu, Y.; Li, H. Automatic Lip-Reading System Based on Deep Convolutional Neural Network and Attention-Based Long Short-Term Memory. *Appl. Sci.* **2019**, *9*, No. 1599.

(6) Lu, L.; Yu, J.; Chen, Y.; Liu, H.; Zhu, Y.; Kong, L.; Li, M. Lip Reading-Based User Authentication Through Acoustic Sensing on Smartphones. *IEEE ACM Trans. Networking* **2019**, *27*, 447−460.

(7) Gogurla, N.; Kim, Y.; Cho, S.; Kim, J.; Kim, S. Multifunctional and Ultrathin Electronic Tattoo for On-Skin Diagnostic and Therapeutic Applications. *Adv. Mater.* **2021**, *33*, No. 2008308.

(8) Kireev, D.; Ameri, S. K.; Nederveld, A.; Kampfe, J.; Jang, H.; Lu, N.; Akinwande, D. Fabrication, characterization and applications of graphene electronic tattoos. *Nat. Protoc.* **2021**, *16*, 2395−2417.

(9) Yu, H.; Bian, J.; Chen, F.; Ji, J.; Huang, Y. Ultrathin, Graphene-in-Polyimide Strain Sensor via Laser-Induced Interfacial Ablation of Polyimide. *Adv. Electron. Mater.* **2022**, No. 2201086.

(10) Pu, Z.; Zhang, X.; Yu, H.; Tu, J.; Chen, H.; Liu, Y.; Su, X.; Wang, R.; Zhang, L.; Li, D. A thermal activated and differential self-calibrated flexible epidermal biomicrofluidic device for wearable accurate blood glucose monitoring. *Sci. Adv.* **2021**, *7*, No. 0199.

(11) Ramírez, J.; Rodriquez, D.; Urbina, A. D.; Cardenas, A. M.; Lipomi, D. J. Combining High Sensitivity and Dynamic Range: Wearable Thin-Film Composite Strain Sensors of Graphene, Ultrathin Palladium, and PEDOT: PSS. *ACS Appl. Nano Mater.* **2019**, *2*, 2222−2229.

(12) Pu, J.-H.; Zhao, X.; Zha, X.-J.; Li, W.-D.; Ke, K.; Bao, R.-Y.; Liu, Z.-Y.; Yang, M.-B.; Yang, W. A strain localization directed crack control strategy for designing MXene-based customizable sensitivity and sensing range strain sensors for full-range human motion monitoring. *Nano Energy* **2020**, *74*, No. 104814.

(13) Zhang, Y.; Chen, L.; Xie, M.; Zhan, Z.; Yang, D.; Cheng, P.; Duan, H.; Ge, Q.; Wang, Z. Ultra-fast programmable human-machine interface enabled by 3D printed degradable conductive hydrogel. *Mater. Today Phys.* **2022**, *27*, No. 100794.

(14) Yang, G.; Yang, Y.; Chen, T.; Wang, J.; Ma, L.; Yang, S. Graphene/MXene composite aerogels reinforced by polyimide for pressure sensing. *ACS Appl. Nano Mater.* **2022**, *5*, 1068−1077.

(15) Yin, R.; Wang, D.; Zhao, S.; Lou, Z.; Shen, G. Wearable Sensors-Enabled Human-Machine Interaction Systems: From Design to Application. *Adv. Funct. Mater.* **2021**, *31*, No. 2008936.

(16) Yu, H.; Gai, M.; Liu, L.; Chen, F.; Bian, J.; Huang, Y. Laser-induced direct graphene patterning: from formation mechanism to flexible applications. *Soft. Sci.* **2023**, *3*, No. 4.

(17) Qiu, Y.; Tian, Y.; Sun, S.; Hu, J.; Wang, Y.; Zhang, Z.; Liu, A.; Cheng, H.; Gao, W.; Zhang, W.; Chai, H.; Wu, H. Bioinspired, multifunctional dual-mode pressure sensors as electronic skin for decoding complex loading processes and human motions. *Nano Energy* **2020**, *78*, No. 105337.

(18) Xia, K.; Xu, Z. Applying a triboelectric nanogenerator by using facial mask for flexible touch sensor. *Sens. Actuators, A* **2021**, *331*, No. 112710.

(19) Zhao, Y.; Huang, Y.; Hu, W.; Guo, X.; Wang, Y.; Liu, P.; Liu, C.; Zhang, Y. Highly sensitive flexible strain sensor based on threadlike spandex substrate coating with conductive nanocomposites for wearable electronic skin. *Smart Mater. Struct.* **2019**, *28*, No. 035004.

(20) Cheng, L.; Qian, W.; Wei, L.; Zhang, H.; Zhao, T.; Li, M.; Liu, A.; Wu, H. A highly sensitive piezoresistive sensor with interlocked graphene microarrays for meticulous monitoring of human motions. *J. Mater. Chem. C* **2020**, *8*, 11525−11531.

(21) Sekikawa, K.; Moriyama, H.; Miyaso, H.; Osada, T.; Ueno, R.; Otsuka, N.; Itoh, M. Evaluation of Yanagihara facial nerve grading system based on a muscle fiber analysis of human facial muscles. *Eur. Arch. Oto-Rhino-Laryngol.* **2019**, *276*, 2055−2060.

(22) Kaidarova, A.; Alsharif, N.; Oliveira, B. N. M.; Marengo, M.; Geraldi, N. R.; Duarte, C. M.; Kosel, J. Laser-Printed, Flexible Graphene Pressure Sensors. *Global Chall.* **2020**, *4*, No. 2000001.

(23) Zhang, H.; He, R.; Niu, Y.; Han, F.; Li, J.; Zhang, X.; Xu, F. Graphene-enabled wearable sensors for healthcare monitoring. *Biosens. Bioelectron.* **2022**, *197*, No. 113777.

(24) Ye, R.; Tour, J. M. Graphene at Fifteen. *ACS Nano* **2019**, *13*, 10872−10878.

(25) Wu, D.; Wang, M.; Zeng, J.; Yao, J.; Jia, C.; Zhang, H.; Li, J. Preparation and Characterization of Graphene from Refined Benzene Extracted from Low-Rank Coal: Based on the CVD Technology. *Molecules* **2021**, *26*, No. 1900.
(26) Huang, G.; Lv, C.; He, J.; Zhang, X.; Zhou, C.; Yang, P.; Tan, Y.; Huang, H. Study on Preparation and Characterization of Graphene Based on Ball Milling Method. *J Nanomater* **2020**, *2020*, No. 2042316.
(27) Huang, L.; Su, J.; Song, Y.; Ye, R. Laser-Induced Graphene: En Route to Smart Sensing. *Nano-Micro. Lett.* **2020**, *12*, No. 157.
(28) Aga, R. S.; Webb, T. M.; Pandhi, T.; Aga, R.; Estrada, D.; Burzynski, K. M.; Bartsch, C. M.; Heckman, E. M. Laser-defined graphene strain sensor directly fabricated on 3D-printed structure. *Flexible Printed Electron.* **2021**, *6*, No. 032001.
(29) Suzuki, K.; Nakagawa, R.; Zhang, Q.; Miura, H. Development of Highly Sensitive Strain Sensor Using Area-Arrayed Graphene Nanoribbons. *Nanomaterials* **2021**, *11*, No. 1701.
(30) Yi, N.; Cheng, Z.; Li, H.; Yang, L.; Zhu, J.; Zheng, X.; Chen, Y.; Liu, Z.; Zhu, H.; Cheng, H. Stretchable, ultrasensitive, and low-temperature NO_2 sensors based on MoS_2@rGO nanocomposites. *Mater. Today Phys.* **2020**, *15*, No. 100265.
(31) Zhu, J.; Liu, S.; Hu, Z.; Zhang, X.; Yi, N.; Tang, K.; Dexheimer, M. G.; Lian, X.; Wang, Q.; Yang, J.; Gray, J.; Cheng, H. Laser-induced graphene non-enzymatic glucose sensors for on-body measurements. *Biosens. Bioelectron.* **2021**, *193*, No. 113606.
(32) Han, R.; Wang, L.; Tang, X.; Qian, J.; Yu, J.; Chen, X.; Huang, Y. Facile fabrication of rGO/LIG-based temperature sensor with high sensitivity. *Mater. Lett.* **2021**, *304*, No. 130637.
(33) Pinheiro, T.; Silvestre, S.; Coelho, J.; Marques, A. C.; Martins, R.; Sales, M. G. F.; Fortunato, E. Laser-Induced Graphene on paper toward efficient fabrication of flexible, planar electrodes for electrochemical sensing. *Adv. Mater. Interfaces* **2021**, *8*, No. 2101502.
(34) Jung, H.; Chun, S.; Kim, Y.; Oh, H. S.; Bae, G. Y.; Bae, G.; Park, W. Fabrication of a Flexible Graphene Pressure Sensor. *J. Nanosci. Nanotechnol.* **2015**, *15*, 9020−9024.
(35) Tian, H.; Shu, Y.; Cui, Y.; Mi, W.; Yang, Y.; Xie, D.; Ren, T. Scalable fabrication of high-performance and flexible graphene strain sensors. *Nanoscale* **2014**, *6*, 699−705.
(36) Chen, Y.; Long, J.; Zhou, S.; Shi, D.; Huang, Y.; Chen, X.; Gao, J.; Zhao, N.; Wong, C.-P. UV Laser-Induced Polyimide-to-Graphene Conversion: Modeling, Fabrication, and Application. *Small Methods* **2019**, *3*, No. 1900208.
(37) Carvalho, A. F.; Fernandes, A. J. S.; Leitão, C.; Deuermeier, J.; Marques, A. C.; Martins, R.; Fortunato, E.; Costa, F. M. Laser-Induced Graphene Strain Sensors Produced by Ultraviolet Irradiation of Polyimide. *Adv. Funct. Mater.* **2018**, *28*, No. 1805271.
(38) Zhang, Y.; Ren, H.; Chen, H.; Chen, Q.; Jin, L.; Peng, W.; Xin, S.; Bai, Y. Cotton fabrics decorated with conductive graphene nanosheet inks for flexible wearable heaters and strain sensors. *ACS Appl. Nano Mater.* **2021**, *4*, 9709−9720.
(39) Murray, R.; Burke, M.; Iacopino, D.; Quinn, A. J. Design of Experiments and Optimization of Laser-Induced Graphene. *ACS Omega* **2021**, *6*, 16736−16743.
(40) Beckham, J. L.; Li, J. T.; Stanford, M. G.; Chen, W.; McHugh, E. A.; Advincula, P. A.; Wyss, K. M.; Chyan, Y.; Boldman, W. L.; Rack, P. D.; Tour, J. M. High-Resolution Laser-Induced Graphene from Photoresist. *ACS Nano* **2021**, *15*, 8976−8983.
(41) Mikheev, K. G.; Zonov, R. G.; Mogileva, T. N.; Fateev, A. E.; Mikheev, G. M. Optical anisotropy of laser-induced graphene films. *Opt. Laser Technol.* **2021**, *141*, No. 107143.
(42) Sun, Z.; Raji, A.-R. O.; Zhu, Y.; Xiang, C.; Yan, Z.; Kittrel, C.; Samuel, E. L. G.; Tour, J. M. Large-Area Bernal-Stacked Bi-, Tr-, and Tetralayer Graphene. *ACS Nano* **2012**, *6*, 9790−9796.
(43) Zhu, C.; Tao, L.; Peng, Z.; Wang, G.; Huang, Y.; Zou, S.; Sun, H.; Zhao, Y.; Chen, X.; Ren, T. An Integrated Luminescent Information Encryption-Decryption and Anticounterfeiting Chip Based on Laser Induced Graphene. *Adv. Funct. Mater.* **2021**, *31*, No. 2103255.
(44) Zhu, C.; Tao, L.; Wang, Y.; Zheng, K.; Yu, J.; L, X.; Chen, X.; Huang, Y. Graphene oxide humidity sensor with laser-induced graphene porous electrodes. *Sens. Actuators, B* **2020**, *325*, No. 128790.
(45) Barbhuiya, N. H.; Singh, S. P.; Makovitzki, A.; Narkhede, P.; Oren, Z.; Adar, Y.; Lupu, E.; Cherry, L.; Monash, A.; Arnusch, C. J. Virus Inactivation in Water Using Laser-Induced Graphene Filters. *Materials* **2021**, *14*, No. 3179.
(46) Kuncoro, R. D. K.; Sugiharti, E. Improved accuracy of recognizing of low-quality face images using two directional matrix in 2D-PCA algorithms and euclidean distance. *J. Phys.: Conf. Ser.* **2021**, *1918*, No. 042142.
(47) Breiding, P.; Sottile, F.; Woodcock, J. Euclidean Distance Degree and Mixed Volume. *Found. Comput. Math.* **2022**, *22*, 1743−1765.
(48) Li, H. Time works well: Dynamic time warping based on time weighting for time series data mining. *Inf. Sci.* **2021**, *547*, 592−608.
(49) Li, Z.; Zhang, F.; Nie, F.; Li, H.; Wang, J. Speed up dynamic time warping of multivariate time series. *J. Intell. Fuzzy Syst.* **2019**, *36*, 2593−2603.
(50) Li, H.; Wang, C. Similarity Measure Based on Incremental Warping Window for Time Series Data Mining. *IEEE Access* **2019**, *7*, 3909−3917.

https://doi.org/10.1021/acsanm.3c00410
ACS Appl. Nano Mater. 2023, 6, 7290−7298